Multi-channel dynamics in high harmonic generation of aligned CO_2: *ab initio* analysis with time-dependent B-spline algebraic diagrammatic construction

M. Ruberti,[*a] P. Decleva,[b] and V. Averbukh[a]

Here we present a fully *ab initio* study of the high-order harmonic generation (HHG) spectrum of aligned CO_2 molecules. The calculations have been performed by using the molecular time-dependent (TD) B-spline algebraic diagrammatic construction (ADC) method. We quantitatively study how the sub-cycle laser-driven multi-channel dynamics, as reflected in the position of the dynamical minimum in the HHG spectrum, is affected by the full inclusion of both correlation-driven and laser-driven dipole interchannel couplings. We calculate channel-resolved spectral intensities as well as the phase differences between contributions of the different ionization-recombination channels to the total HHG spectrum. Our results show that electron correlation effectively controls the relative contributions of the different channels to the total HHG spectrum, leading to the opening of the new ones ($1^2\Pi_u$, $1^2\Sigma_g^+$), previously disregarded for the aligned molecular setup. We conclude that inclusion of many-electron effects into the theoretical interpretation of molecular HHG spectra is essential in order to correctly extract ultrafast electron dynamics using HHG spectroscopy.

1 Introduction

The groundbreaking development of the attosecond laser pulses [1] in the extreme ultraviolet (XUV) spectrum where atoms and molecules can be ionized has enabled the experimental study of attosecond physics [2]. Time-domain studies of electronic motion in atoms, molecules and the condensed phase offer new approaches to understanding electronic structure and correlations [3–14]. In particular HHG spectroscopy [15–18], which relies upon measuring the spectrum of coherent radiation emitted by molecules aligned in space when interacting with intense laser fields, has proven to be a powerful technique to resolve ultrafast electron dynamics in molecules with the potential for subangstrom spatial resolution and subfemtosecond temporal resolution [19–27]. It has often been assumed that structures in the harmonic spectra reflect the geometry of the highest occupied molecular orbital (HOMO) [19,21,28–35]. Indeed, strong-field ionization is exponentially sensitive to the ionization potential I_p, suggesting that after ionization the molecular ion is left in its ground electronic state (electron removal from HOMO in the Hartree-Fock picture). In this case, even though rearrangement has occurred, only structural information will be recorded in the harmonic spectrum. However, in molecular ions, electronic excitations often lie within a couple of electron volts from the ground state, leading to sizeable population amplitudes even for exponential scaling of ionization rates. The geometry of the molecular orbitals is also crucial [36,37] and can further increase relative populations of the excited electronic states of the ion (tunnelling from deeper orbitals in the Hartree-Fock picture). The importance of different ionization channels in high harmonic generation has been pointed out in various experiments [38,39]. Moreover, clear evidence for strong-field ionization from lower orbitals has demonstrated the importance of including multiple orbitals in the description of HHG [25,38,40] similar to inclusion of multiple excited states of the neutral for particular molecular systems [41] and pre-excited atoms [42].

Different states of the molecular ion populated between ionization and recombination provide different channels for the HHG process. These channels are different pathways that take the system from one initial state to the same final state via different states of the ion and, for each channel, specific electronic structure and ultrafast laser sub-cycle dynamics are encoded onto the amplitude and the phase of the harmonic emission signal. The coherent sum of the multiple channels can thus reveal both structural minima due to the recombination matrix elements or dynamical minima that occur because of destructive interferences between channels. Their interference records the relative phases between the channels by mapping them onto the amplitude modulation in the harmonic spectra. Therefore the ability to correctly predict the position of the dynamical minima and their mobility with respect to the laser field parameters is essential for the reconstruction of field induced attosecond many-electron dynamics [25].

If the minimum is structural as in argon [43], its position is largely

[a] *Department of Physics, Imperial College London, Prince Consort Road, London SW7 2AZ, United Kingdom. Tel: 0044 20 7589 47728; E-mail: m.ruberti11@imperial.ac.uk*
[b] *Dipartimento di Scienze Chimiche, Universita' di Trieste, Via Giorgieri 1, I-34127 Trieste, Italy*

independent of the laser parameters including wavelength and intensity[28,44–48]. If the minimum is dynamical, as in CO_2[21], the interference of the orbitals can be controlled directly by the intensity and the wavelength of the IR driving laser field. In addition to the relative phase that different channels accumulate between ionization and recombination, the structure of the orbitals can lead to a significant phase variation in the recombination matrix element that also affects the observed minimum position. In the harmonic spectrum of the CO_2 molecule, minima have been found at vastly different positions in different experiments[21,29–31,49]. A spectral minimum observed in CO_2 molecules aligned parallel to the generating laser field was found at 39 eV in[21], at 54 eV in[29], and in a range of intermediate positions, depending on the intensity, in[25,49].

The two most common theoretical approaches for describing molecular HHG are the semiclassical strong-field approximation (SFA)[50], which has been extended to include Coulomb-interaction corrections[44,51–55], and the single-active-electron (SAE) approximation[56–60], where the electron-ion interaction for many-electron systems is described by a model potential[58]. A number of theoretical works based on the SFA approximation and on extensions of this have been performed during the last few years. While most recent works indicate that the ionization from multiple orbitals (HOMO and HOMO-2) is responsible for the intensity dependence of the minimum position[25], other works suggested that either the effect of the strong laser field on a single orbital can explain the intensity dependence[21,29,30,61] in CO_2 molecules aligned parallel to the driving field, or that both the interference of multiple orbitals and their structural characteristics can affect the position of the minimum[49,62]. The results presented in[49] show that in addition to the interference of multiple orbitals (HOMO and HOMO-2), the structure of the highest occupied molecular orbital (HOMO) affects the position of the minimum. Indeed, the interference of the recombining electron with the 2-centre HOMO results in a strong phase variation of the recombination matrix element with respect to the emitted photon energy. It is now generally recognised that the minimum present in the HHG spectrum of CO_2 has a dynamical nature and is the result of the fact that more than one ionization channel contributes to the total HHG intensity spectrum. Therefore the study of its position and mobility offers the opportunity to extract the attosecond many-electron dynamics induced in the CO_2 parent ion between the ionization and recombination events.

The important role of couplings between the ionization channels due to correlation-driven interactions during tunnelling, propagation and recombination of the liberated electron, whose accurate description requires an *ab initio* approach, in the characterization of the sub-cycle laser-driven dynamics between CO_2 cationic states upon strong field ionization has been recently discussed and pointed out in[63]. Correlation-assisted optical tunnelling has been first described in[55] and[64]. However, finding signatures of this process in standard observables such as angle-resolved photo-electron spectra has proved to be elusive. Recently, in[63], it has been argued that such signatures were observed in high harmonic generation by CO_2 molecules. However, the role of correlation assisted tunnelling was only inferred. *Ab initio* studies of the effect of correlation-driven interchannel couplings onto the HHG spectra have been performed in atomic systems[65,66] showing how the inclusion of these couplings can quantitatively explain some of the features observed in the measured atomic HHG spectra. However, although multi-orbital and many-body effects are especially relevant in molecules[25,38,67] due to the much smaller energy separation between the eigenstates of the ionic system with respect to the atomic case, no fully *ab initio* studies of the effects of many-electron correlation-driven interchannel couplings onto molecular HHG spectra have been performed so far.

In this work we solve, fully *ab-initio*, the 3D molecular many-electron time-dependent Schrödinger equation for the CO_2 molecule interacting with a high-intensity ultra-short infrared (IR) laser pulse, calculating the HHG spectra for a set of different laser field intensities and quantitatively investigating the effect of its multi-channel nature on the position, contrast and mobility of the dynamical minimum. The calculation has been performed using our molecular B-spline time-dependent algebraic diagrammatic construction (B-spline TD-ADC) fully *ab initio* tool, which is based on the many-body Green's function ADC methods[68–70], B-spline basis set[43] and Arnoldi-Lanczos time propagation algorithm[71]. Specifically, in the following study, the first order ADC(1) scheme of the ADC(n) hierarchy has been used for the description of the CO_2 many-electron wave-function. Our aim is to study, for the first time using a completely *ab initio* 3D method for this purpose, whether and the extent to which the many-electron correlation-driven interchannel couplings affect the sub-cycle attosecond dynamics of the various molecular ionization channels, including the electron rearrangement within the parent ion. This is important in order to understand the relevance of interchannel couplings for HHG spectroscopy, i.e. the importance of their theoretical modeling in the analysis and interpretation of the molecular HHG spectra in order to correctly extract information about the time-resolved attosecond electron dynamics of the system. Moreover, beside understanding how the multi-channel ultrafast electron dynamics behind the HHG emission process in aligned CO_2 molecules is modified by the inclusion of correlation-driven interchannel couplings, including the possibility for more ionization channels, other than HOMO and HOMO-2, to substantially contribute to the total CO_2 HHG spectrum, we are also interested in comparing the experimental results with our *ab initio* theory results on the dynamical minima positions and intensity dependence.

This article is organized as follows. The relevant aspects of the B-spline ADC approach to molecular excited states together with a general description of its time dependent (TD) implementation which is based on the use of the Arnoldi-Lanczos numerical algorithm for the wavepacket time propagation calculations are presented in Sec. 2. In Section 3, the multi-channel effects on the dynamical minimum present in the total CO_2 HHG spectrum are quantitatively investigated. In Section 4, channel-resolved spectra are calculated and the dependence of their relative contributions and interferences onto the interchannel couplings is investigated. Conclusions are given in Section 5.

2 ADC *ab initio* schemes within the intermediate state representation

The calculation presented in this work have been performed using a fully *ab initio* tool developed by us for solving the 3D molecular many-electron time-dependent Schrödinger equation for the neutral molecular system interacting with the laser field, molecular B-spline time-dependent algebraic diagrammatic construction (B-spline TD-ADC) that is based on the many-body Green's function ADC schemes[68–70], B-spline basis set[43] and Arnoldi-Lanczos time propagation algorithm[71].

A rigorously accurate study of molecular HHG spectra has to rely upon the inclusion of all the couplings between the ionisation-recombination channels possibly participating to the ultrafast electron dynamics, especially in order to understand the nature of dynamical minima present in the spectra, whose position and mobility inherently reflects the laser-driven sub-cycle multi-channel dynamics. The possibility for different final states of the molecular ion to produce HHG signal provides a basis for recording many-electron dynamics, including dynamics of electron rearrangement upon ionization. The phases between the channels, accumulated between ionization and recombination, encode the underlying electronic dynamics with attosecond time resolution, including the Coulomb interaction between the excited electron and the parent ion. The nature of this interaction can be understood as the sum of two different contributions. The first contribution refers to the interaction of the liberated electron with the ionic hole state, from which it originates, and is referred to as intrachannel interaction leading for large electron-ion distances to the $1/r$ behaviour of the Coulomb potential. This residual electron-ion intrachannel interaction is described in detail within the ADC schemes, including multipole effects to infinite order and therefore going beyond the limitations of any single-active-electron (SAE) approximation[56–60], where the intrachannel electron-ion interaction is described by a model potential. The second contribution describes the case where the liberated electron is influenced by other molecular orbitals (channels) and it is referred to as correlation-driven interchannel coupling[72]. Interchannel couplings can change the state of both the ionised electron and the parent ion during the laser-driven sub-cycle electron dynamics. Within the ADC schemes, both couplings between the different ionisation channels contributing to the HHG spectrum, the one induced by the laser electric field

$$D_{ai,bj}E(t) = -\delta_{a,b}\langle i \mid \hat{d} \mid j\rangle E(t)\; i \neq j\,, \tag{1}$$

consisting of the electron rearrangement within the ion caused by laser-driven dipole couplings between the different ionic states i and j, and the one induced by the full Coulomb interaction

$$H^{[1]}_{ai,bj} = -V_{aj[bi]} = -\langle aj \,||\, bi\rangle \; i \neq j\,, \tag{2}$$

, consisting of many-electron dynamics induced by the correlation-driven interchannel couplings, are taken into account. In Eqs. (1,2) a and b represent the photo-electron degree of freedom while $H^{[1]}_{ai,bj} = -V_{aj[bi]}$ represents the matrix element of the two-particle Coulomb interaction included in the full molecular electronic Hamiltonian. Both couplings affect the interference pattern in the total HHG spectrum, which originates from the different phases and intensities of the various harmonic emission channels. While the couplings driven by the electric field can be included into the SFA approach, Coulomb correlation-driven interchannel couplings[72] go beyond the independent-electron picture and are not captured within the framework of neither SFA[44,50–55] nor SAE methods[56–60].

Within our approach the many-electron correlated states are described by the ADC *ab initio* schemes[68]. The starting point of the intermediate states representation (ISR) approach to the hierarchy of the ADC schemes[73,74] is the construction of the so-called correlated excited states (CES), defined as

$$\mid \Psi^0_I\rangle = \hat{C}^\dagger_I \mid \Psi_0\rangle\,, \tag{3}$$

where the operators $\hat{C}^\dagger_I$ denote the physical excitation operators corresponding respectively to 1p1h, 2p2h etc... excitations,

$$\hat{C}^\dagger_I = \left\{\hat{a}^\dagger_a\hat{a}_i\,;\, \hat{a}^\dagger_a\hat{a}^\dagger_b\hat{a}_j\hat{a}_k \;\; (a<b, j<k)\,\ldots\ldots\right\}, \tag{4}$$

and $\mid \Psi_0\rangle$ is the exact correlated ground state of the system.

This non-orthogonal CES basis set is complete in the space of the excited states of the N-electron system[75] and has the advantage that ground state correlation is already built into every basis vector. It can be orthonormalized in a two-step procedure. First, one performs Gram-Schmidt orthogonalization of each excitation class with respect to all the lower excitation classes. The states $\mid \Psi^{m\#}_y\rangle$ formed in this first step are referred to as precursor states. The second step is symmetric orthonormalization of the resulting precursor states within each excitation class. As an example the procedure for the first (1h1p) excitation class gives the following precursor states:

$$\mid \Psi^{1\#}_{ai}\rangle = \hat{a}^\dagger_a\hat{a}_i \mid \Psi_0\rangle - \mid \Psi_0\rangle\langle\Psi_0 \mid \hat{a}^\dagger_a\hat{a}_i \mid \Psi_0\rangle\,. \tag{5}$$

The second step gives

$$\mid \tilde{\Psi}^1_{ai}\rangle = \sum_{bj} \mid \Psi^{1\#}_{bj}\rangle \left(S^{-\frac{1}{2}}\right)_{bj,ai}\,, \tag{6}$$

where $\mathbf{S}$ is the overlap matrix of the first excitation class precursor states, i.e.

$$S_{bj,ai} = \langle \Psi^{1\#}_{bj} \mid \Psi^{1\#}_{ai}\rangle \tag{7}$$

In a compact notation the excitation class orthogonalized (ECO) states can be written as

$$\mid \tilde{\Psi}^m_x\rangle = \hat{Q}^{m-1}\sum_y \mid \Psi^m_y\rangle \left(S^m_{yx}\right)^{-12}\,, \tag{8}$$

where S^m_{yx} is defined as

$$S^m_{yx} = \langle \Psi^m_y \mid \hat{Q}^{m-1} \mid \Psi^m_x\rangle \tag{9}$$

and

$$\hat{Q}^m = \hat{1} - \sum_{l=0}^{m}\hat{P}^l \tag{10}$$

is the projector operator onto the space orthogonal to the first m excitation classes. Finally, every intermediate state can be ex-

pressed as

$$|\,\tilde{\Psi}_I\rangle = \tilde{C}_I^{\dagger}\,|\,\Psi_0\rangle\,, \tag{11}$$

where all the effects of the consecutive orthonormalizations are encoded in the new creation operators $\tilde{C}_I^{\dagger}$.

The ADC secular matrix is the representation of the shifted electronic Hamiltonian operator $\hat{H}-E_0$ in the ECO-CES space:

$$\mathscr{H}_{IJ} = \langle\tilde{\Psi}_I\,|\,\hat{H}-E_0\,|\,\tilde{\Psi}_J\rangle = \langle\Psi_0\,|\,\tilde{C}_I\left[\hat{H},\tilde{C}_J^{\dagger}\right]\,|\,\Psi_0\rangle\,. \tag{12}$$

At this point Møller-Plesset (MP) perturbation theory[76] is introduced to describe the ground state correlation, i.e. $|\,\Psi_0\rangle$ and E_0:

$$|\,\Psi_0^{'}\rangle = |\,\Phi_0^{HF}\rangle + |\,\Psi_0^{[1]'}\rangle + |\,\Psi_0^{[2]'}\rangle + |\,\Psi_0^{[3]'}\rangle + \ldots\,, \tag{13}$$

where the first order correction $|\,\Psi_0^{[1]'}\rangle$ contains only double excitations (2h2p), while $|\,\Psi_0^{[2]'}\rangle$ contains single, double, triple and quadruple excitations with respect to $|\,\Phi_0^{HF}\rangle$.

The vertical excitation energies are obtained by solving the eigenvalue problem $\mathbf{HV}=\omega\mathbf{V}$, and the excited eigenstates of the system are therefore given, in the basis of the intermediate states, as:

$$|\,\Psi_n\rangle = \sum_I V_{I,n}\,|\,\tilde{\Psi}_I\rangle\,. \tag{14}$$

Using this explicit expression for the excited states of the system, one contains the corresponding transition moments as

$$\langle\Psi_m\,|\,\hat{D}\,|\,\Psi_0\rangle = \mathbf{V}_m^{\dagger}\cdot\mathbf{F} = \sum_{rs} d_{rs}\mathbf{V}_m^{\dagger}\cdot\mathbf{f}_{rs}\,, \tag{15}$$

where d_{rs} are the matrix elements of the dipole operator on the one particle orbitals chosen as basis set functions. The matrix of effective transition amplitudes $\mathbf{f}$ and the associated vector $\mathbf{F}$ are defined by:

$$f_{I,rs} = \langle\tilde{\Psi}_I\,|\,\hat{a}_r^{\dagger}\hat{a}_s\,|\,\Psi_0\rangle\,,\quad F_I = \langle\tilde{\Psi}_I\,|\,\hat{D}\,|\,\Psi_0\rangle\,. \tag{16}$$

The hierarchy of ADC(n) approximations is obtained for each order n by truncating the intermediate state manifold at some limiting excitation class and, also, by truncating the resulting perturbation expansions for the included classes in the way consistent with the polarization propagator approach. For example, at the ADC(2) level, the Hamiltonian matrix of the system can be represented as

$$\mathbf{H}^{\mathrm{ADC}[2]} = \mathbf{H}^{[0]} + \mathbf{H}^{1,1[1]} + \mathbf{H}^{1,1[2]} + \mathbf{H}^{1,2[1]} + \\ + \mathbf{H}^{2,1[1]}$$

where $\mathbf{H}^{i,j[N]}$ denotes the ipih-jpjh excitations block of the Hamiltonian computed at the order N of perturbation theory.

Thus, in ADC(2) the perturbation expansion of the secular matrix elements extends through second, first and zero-th order in the 1h1p block, the 1h1p-2h2p coupling block and the diagonal 2h2p block, respectively. In a similar way the 1h1p and 2h2p parts of the effective transition amplitudes are given by perturbation expansions through second and first order respectively. An extension of the ADC scheme, not strictly consistent with the polarization propagator and referred to as ADC(2) extended [ADC(2)x], is obtained by using the first order expansion for the 2h2p block that accounts for the couplings between the 2h2p intermediate states. The ADC(n) schemes are size consistent and compact relative to the corresponding truncated CI expansions[77–79]. The dipole matrix between the excited states of the system is constructed in the same way and can be represented as

$$\mathbf{D}^{\mathrm{ADC}[2]} = \mathbf{D}^{[0]} + \mathbf{D}^{1,1[1]} + \mathbf{D}^{1,1[2]} + \mathbf{D}^{1,2[1]} + \\ + \mathbf{D}^{2,1[1]}\,.$$

In the ADC(1) scheme the Hamiltonian reduces to the configuration interaction singles (CIS) one, while the transition moment with respect to the ground state are expressed as

$$\langle\tilde{\Psi}_i^a\,|\,\hat{D}\,|\,\Psi_0\rangle = d_{ai} + \sum_v\sum_o \frac{\langle va\,||\,oi\rangle}{\varepsilon_o+\varepsilon_i-\varepsilon_v-\varepsilon_a} d_{ov} \tag{19}$$

where $\langle va\,||\,oi\rangle$ is the antisymmetrized two-particle Coulomb integral in physicists' notation and the two indeces v and o run over the virtual and the occupied canonical (Hartree-Fock) orbitals respectively.

Monocentric B-spline basis[80], which is composed of a spherical harmonics for the angular part and B-splines for the radial coordinate, is used to represent single particle orbitals which are therefore expressed as

$$\psi_{ilm} = \frac{1}{r}B_i(r)Y_{lm}(\theta,\phi). \tag{20}$$

Here we work with B-splines of order 10 and the B-spline knot sequence we use is the parabolic-linear sequence[43], which is a mix of these two types of sequences: a short-range dense one which concentrates points near the nucleus with quadratically increasing knot spacing and a linear knot spacing sequence for larger values of r necessary for continuum states description.

Within TD-ADC, the many-electron time-dependent Schrödinger equation (TDSE) is solved making the following ansatz for the time-dependent electronic wave-function:

$$|\,\Psi(t)\rangle = C_0(t)\,|\,\Psi_0\rangle + \sum_I C_I(t)\,|\,\tilde{\Psi}_I\rangle \tag{21}$$

where the coefficients $C_0(t)$ and $C_I(t)$ refer to the ground-state and to the ECO-CES ADC configuration basis states respectively. Propagation of the B-spline ADC many-electron wave-function allows one to achieve a realistic *ab-initio* description of a series of many-electron phenomena in the time-resolved fashion on the atto- and femto-second scale. In this work, a complex absorbing potential (CAP)[81] has been used in order to eliminate wavepacket reflection effects from the radial grid boundaries. With the addition of a complex-absorbing potential, the Hamiltonian becomes complex symmetric. The time propagation of the unknown coefficients C_0, C_n of the B-spline ADC many-electron wave-function is performed by means of the general complex Lanczos, or Arnoldi-Lanczos, algorithm[82–84]. The Lanczos algorithm has been proved to be very efficient as a time propagation scheme for the non-relativistic Schrödinger equation[85] and is widely used in treating nuclear-dynamics problems[71,86,87]. The more general Arnoldi-Lanczos algorithm is suited to describe time-propagation with

non-Hermitian Hamiltonians as well as the usual Hermitian ones and it can be used efficiently for complex symmetric Hamiltonians.

It is known that the time-dependent Schrödinger equation has a formal solution

$$| \Psi(t)\rangle = \hat{U}(t,0) \mid \Psi(0)\rangle = \tag{22}$$

$$T \exp\left(-\frac{i}{\hbar}\int_0^t \hat{H}(t^{'})dt^{'}\right) \mid \Psi(0)\rangle .$$

where T exp is the so-called chronological exponent which represents the evolution operator $\hat{U}(t,0)$.

For a sufficiently small time increment Δt, over which the variation of the Hamiltonian is negligible, the evolution operator describing the evolution of the system from time t to time $t+\Delta t$ can be written as

$$\hat{U}(\Delta t) = \hat{U}(t+\Delta t, t) = \exp\left(-\frac{i}{\hbar}\hat{H}\Delta t\right). \tag{23}$$

The Arnoldi-Lanczos algorithm leads to the following polynomial expansion of the exponential in the evolution operator:

$$\hat{U}(\Delta t) \approx \sum_{j=1}^{K} c_j P_j\left(-\frac{i}{\hbar}\hat{H}\Delta t\right) \tag{24}$$

where $P_j\left(-\frac{i}{\hbar}\hat{H}\Delta t\right)$ is a polynomial of degree j, and c_j are the expansion coefficients.

This polynomial expansion is obtained by projecting the Hamiltonian of the system at time t onto the Krylov subspace constructed starting from the normalised state vector of the system at the same time t, i.e. $\mathbf{V}_0 = \psi(t)$, and spanned by the vectors $\mathbf{V}_j = \mathbf{H}^j\psi(t) \quad j = 0,1,2,\ldots,K-1$. Here $\mathbf{H}$ and $\psi(t)$ are respectively the matrix representations of $\hat{H}$ and $| \Psi(t)\rangle$ in the ECO-CES ADC basis.

The recursive procedure for building the reduced Hamiltonian matrix $\mathbf{H}_K$ within the K-dimensional Krylov subspace reads as

$$\tilde{\mathbf{V}}_{j+1}^{(1)} = \mathbf{H}\mathbf{V}_j \tag{25}$$

$$\text{for } i = 1,\ldots..,j$$

$$\beta_{ij} = \mathbf{V}_i^{\dagger}\tilde{\mathbf{V}}_{j+1}^{(i)} \quad \tilde{\mathbf{V}}_{j+1}^{(i+1)} = \tilde{\mathbf{V}}_{j+1}^{(i)} - \beta_{ij}\mathbf{V}_i$$

$$\mathbf{V}_{j+1} = \frac{\tilde{\mathbf{V}}_{j+1}^{(j+1)}}{\beta_{j+1,j}} \quad \beta_{j+1,j} = \| \tilde{\mathbf{V}}_{j+1}^{(j+1)} \| .$$

In this way, starting with a normalised state $\mathbf{V}_0 = \psi(0)$ one constructs an orthonormal basis $\mathbf{V}_0,\ldots,\mathbf{V}_{K-1}$ for the K-dimensional Krylov subspace, which represents a very good approximation to the Hilbert subspace to which the state of the system at time $t+\Delta t$ belongs and in which the reduced Hamiltonian $\mathbf{H}^K$ is represented as a complex upper Hessenberg matrix, i.e. a matrix which has zero entries only below the first subdiagonal,

$$H_{ij}^K = \mathbf{V}_i^{\dagger}\mathbf{H}\mathbf{V}_j = \tag{26}$$

$$= \begin{pmatrix} \beta_{0,0} & \beta_{0,1} & \cdots & \cdots & \beta_{0,K-1} \\ \beta_{1,0} & \ddots & \ddots & \ddots & \vdots \\ 0 & \ddots & \ddots & \ddots & \vdots \\ 0 & 0 & \ddots & \ddots & \beta_{K-2,K-1} \\ 0 & 0 & 0 & \beta_{K-1,K-2} & \beta_{K-1,K-1} \end{pmatrix}.$$

In order to assure numerical orthogonality of the Krylov space basis set, at each step, each state vector is orthogonalised twice with respect to the previous ones. Therefore the final formulas for the reduced Hamiltonian matrix are:

$$\tilde{\mathbf{V}}_{j+1}^{\text{new }(1)} = \tilde{\mathbf{V}}_{j+1}^{(j+1)} \tag{27}$$

$$\text{for } \quad i = 1,\ldots..,j$$

$$\beta_{ij}^{\text{correction}} = \mathbf{V}_i^{\dagger}\tilde{\mathbf{V}}_{j+1}^{\text{new }(i)}$$

$$\tilde{\mathbf{V}}_{j+1}^{\text{new }(i+1)} = \tilde{\mathbf{V}}_{j+1}^{\text{new }(i)} - \beta_{ij}^{\text{correction}}\mathbf{V}_i$$

$$\beta_{ij}^{final} = \beta_{ij}^{standard} + \beta_{ij}^{\text{correction}} .$$

This re-orthogonalization procedure is also known as the Kahan-Parlett "twice is enough" algorithm [88] and provides a very good level of accuracy for the orthogonality of the resulting Krylov basis states.

The propagation operator $\hat{U}(\Delta t)$ can be approximated by its representation in the Krylov subspace:

$$\mathbf{U}_K(\Delta t) = \exp\left(-\frac{i}{\hbar}\mathbf{H}_K\Delta t\right). \tag{28}$$

Consequently the propagated vector we are interested in will be approximated by

$$\Psi(t) \approx \mathbf{U}_K(\Delta t)\Psi(0) . \tag{29}$$

The propagation of the initial wave-function is hence performed in the projected subspace by the upper Hessenberg Hamiltonian $\mathbf{H}_K$, which is much smaller than the full Hamiltonian and therefore much easier to diagonalise. After the diagonalization the propagator can be expressed in the following form:

$$\mathbf{U}_K(\Delta t) = \mathbf{Z}^{\dagger}\exp\left(-\frac{i}{\hbar}\mathbf{D}_K\Delta t\right)\mathbf{Z}, \tag{30}$$

where $\mathbf{Z}$ is the eigenvector matrix of $\mathbf{H}_K$, and $\mathbf{D}_K$ is its diagonal matrix of eigenvalues. The propagated vector is constructed from the eigenvalues and eigenvectors of the matrix $\mathbf{H}_K$ and reads:

$$\Psi(t) = \exp\left(-\frac{i}{\hbar}\mathbf{H}_K\Delta t\right)\Psi(0) = \sum_{j=1}^{K-1} a_j\mathbf{V}_j , \tag{31}$$

where its coefficients onto the Krylov space basis vectors read

$$a_j = \sum_{n=0}^{K-1} Z_{jn}\exp\left(-\frac{i}{\hbar}\lambda_n\Delta t\right)\left(Z^{-1}\right)_{n0} . \tag{32}$$

In Eq. (32) the λ_n denote the eigenvalues of the matrix H_K. The propagated wave-function is then used as the initial vector for the next iteration, Eq. (25).

In the computational implementation of this scheme used in TD B-spline ADC, it is possible to fix the maximum number of iterations requested, i.e. the maximum allowed dimension of the Krylov space. Moreover, the algorithm is stopped when the norm of the $(j+1)$-th Krylov vector candidate becomes smaller than a certain fixed threshold value, which, in this work, has been taken as the numerical precision of the calculator. The error, i.e. the difference between the propagated and exact wave-functions, when using the Lanczos integrator is sensitive to both the time-step size Δt or the maximum order K allowed. All the results presented in this work have been obtained using a value, for both the time-step Δt and the maximum Krylov space dimension allowed K, at which the convergence of the calculated physical quantities has been achieved.

From the computational point of view this complex version of the Lanczos scheme is obviously more time-consuming with respect to the Hermitian version, since in addition to the diagonalization of the reduced Hamiltonian, in this case an upper Hessenberg matrix, one needs to perform an inversion of its eigenvector matrix, $\mathbf{Z}$, which is now not unitary. Nevertheless, for non-Hermitian cases the Lanczos-Arnoldi algorithm appears to be very efficient.

Using this algorithm, the time propagation reduces to repetitive diagonalization, at each time step, of Hessenberg matrices whose dimension is significantly smaller with respect to the full ADC Hamiltonian. This allows the treatment of dynamical problems in which the size of the resulting system Hamiltonian is relatively large and time-propagation by full diagonalization of the secular matrix at each time step becomes practically inaccessible. Another very important feature of the Arnoldi-Lanczos algorithm is that, when computing the tridiagonal matrix $\mathbf{H}_K$, the full Hamiltonian matrix $\mathbf{H}$ is needed only for a simple matrix vector product and remains unchanged during the whole procedure. Each of these reduced single calculations has been massively parallelized, both inter-nodes, with standard MPI (message passing interface) technology in parallel computing environment[89], and intra-node with OpenMP (shared memory) technology[90].

The time propagation can be performed representing the operators matrices both in the ECO-CES configuration basis set or in the Hamiltonian eigenvectors basis set. In the second scheme, after the Hamiltonian has been diagonalised, the dipole and CAP matrices are transformed to their representations in the basis of the Hamiltonian eigenvectors through the following formulae:

$$\mathbf{D}_{eigen} = \mathbf{Z}^{\dagger}\mathbf{D}_{ECO-CES}\mathbf{Z}, \tag{33}$$

$$\mathbf{CAP}_{eigen} = \mathbf{Z}^{\dagger}\mathbf{CAP}_{ECO-CES}\mathbf{Z}. \tag{34}$$

The main advantages of this approach are that the dense Hamiltonian matrices do not have to be stored anymore, reducing the dynamical memory requirements of the calculation. However the CAP matrices will generally become dense and therefore will need to be fully stored. The second advantage of this scheme is that the basis states immediately have a clearer physical interpretation. Indeed, it becomes easier to calculate the rate of ionization caused by the laser pulse, just by looking at the population of the bound eigenstates of the system at the end of the pulse. Therefore, it is not necessary to wait for the whole outgoing ionised wavepacket to be absorbed by the CAP and to look at the resulting loss of norm of the wave-function, as is the case for the first scheme. However, the full diagonalization can be performed with reasonable expense only for relatively small basis sets.

In order to guarantee the convergence of the Arnoldi-Lanczos algorithm, which depends crucially on the spectral radius of the Hamiltonian, in the first propagation scheme we removed from the numerical simulation the ECO-CES configurations with a zeroth-order energy higher than a certain threshold value. In an analogous way, in the second propagation scheme the unphysical high energy eigenstates have been removed from the propagation. The threshold value for the cutoff energy which has been used in the calculations performed in this work is 40 a.u.; with this choice the Arnoldi-Lanczos algortihm converges well at each time step and, moreover, the removal of these high energy electron orbitals has no effect on the HHG spectra we are looking at.

3 ADC(1) calculation of the total HHG spectrum of CO_2: intensity dependence of the dynamical minimum

The first step in the calculation is the solution of the discretised closed-shell Hartree-Fock (HF) equations[43] which, in the molecular case is solved for every irreducible representation (IRREP) of the molecular point symmetry group. In the case of the carbon dioxide molecule, whose point symmetry group is $D_{\infty h}$, the number of spherical harmonics belonging to each IRREP is equal to $L_{max}+1$ for Σ_g and to L_{max} for all the other IRREPS $(\Sigma_u, \Pi_u, \Pi_g, ...)$. Here L_{max} represents the maximum value of the orbital angular momentum used in the calculation, which in this work has been set to be $L_{max} = 60$. Solving the molecular HF equations self-consistently, we obtain a quasi-complete set of canonical occupied and virtual HF molecular orbitals, expressed in terms of B-spline basis functions.

Within the range of ionizing field parameters used in this work, a total of four ionization channels of the CO_2 molecule, corresponding to creating the CO_2 ion in the ground $1^2\Pi_g$ (channel X), first $1^2\Pi_u$ (channel A), second $1^2\Sigma_u^+$ (channel B) and third excited state $1^2\Sigma_g^+$ (channel C) respectively, play the main role in the triggered electron dynamics and contribute to the harmonic emission of the CO_2 molecule, while the contribution of deeper ionization channels was found to be negligible. Within ADC(1) they respectively consist of, in the molecular orbital picture, the removal of a bound electron from the HOMO ($1\pi_g$), HOMO-1 ($1\pi_u$), HOMO-2 ($3\sigma_u$) and HOMO-3 ($4\sigma_g$) occupied HF orbitals. Indeed the orbitals relevant for ionization and recombination are the Dyson orbitals, the overlaps between the many-electron ground state wave-function of the neutral system and the ground/excited state wave-function of the ion and, within the ADC(1) method, they coincide with the occupied HF orbitals of the neutral system[91]. While the corresponding experimental ionization potentials are

respectively 13.8, 17.3, 18.1 and 19.36 eV[92] and therefore span a 5.56 eV energy range, the ADC(1) ionization potentials obtained in this calculation are 15.03, 18.81, 19.6 and 20.7 eV spanning a 5.7 eV energy range. In Table 1 a comparison is shown between the experimental orbital/ionization energies of the CO_2 molecule and the theoretical results obtained by means of HF calculations performed using our B-spline basis set and a cc-pcvTZ Gaussian basis set respectively. The GTO HF calculation was performed using the MOLPRO quantum chemistry package[93].

Table 1 Orbital/ionization energies of the CO_2 molecule. Comparison between the experimental values and the theoretical results obtained by means of HF calculations performed using our B-spline basis set and a cc-pcvTZ Gaussian basis set respectively

Ionic state	Experimental I.P.s (eV)[92]	HF B-spline basis I.P.s (eV)	HF cc-pcvTZ GTO basis I.P.s (eV)
$1^2\Pi_g$	13.8	15.03	14.74
$1^2\Pi_u$	17.3	18.81	19.31
$1^2\Sigma_u^+$	18.1	19.6	20.126
$1^2\Sigma_g^+$	19.36	20.7	21.76

In order to investigate the role of the different channels, and to better understand the effect of their interaction, the HHG spectrum of CO_2 was calculated not only at the full ADC(1) level of *ab-initio* theory, but also at two different levels of approximation. The first level of approximation consists of setting to zero the correlation-driven interchannel coupling of Eq. (2) due to the electron-electron Coulomb interaction and will be referred to as *model-2* in the following; the second and lower level of approximation consists of setting to zero both the correlation-driven interchannel couplings of Eq. (2) and the dipole interchannel couplings of Eq. (1) driven by the ionic dipole transitions induced by the strong IR electric field and will be referred to as *model-3* in the following.

In this work, the many-electron ECO-CES configurations built with the HF orbitals are both spin-adapted and point-symmetry group adapted ones. Therefore we take into account the full symmetry of the molecule, i.e. $D_{\infty h}$, not only in the HF one-particle calculation but also in the many-electron ADC one. Differently from experiments, where the HHG spectrum measured can be considered to be the result of a coherent average over molecular alignment distributions, here the calculation has been performed for CO_2 molecules perfectly aligned along the IR laser field polarization direction. Using a laser field linearly polarised along the molecular axis leads to conservation of the quantum number M representing the total electronic axial angular momentum and, consequently, in the simulations it is enough to consider only the two many-electron spaces corresponding to the irreducible representations Σ_g^+ and Σ_u^+.

The experimental conditions, where the contribution of the 'long trajectories' has been filtered out, are simulated by using a complex absorbing potential (CAP). The form of the CAP used was the following:

$$\hat{W} = \eta(r - r_{CAP})^2 \ , \ r \geq r_{CAP} \tag{35}$$

and with the addition of the CAP term the form of the total time-dependent Hamiltonian of the system reads

$$\hat{H} = \hat{H}_0 + \hat{z}E(t) - i\hat{W} \tag{36}$$

where $\hat{H}_0$ is the field-free many-electron ADC Hamiltonian and $\hat{z}E(t)$ is the laser-atom interaction in length form and within the dipole approximation.

Indeed, in a molecular gas, the propagation of harmonic radiation associated with short and long trajectories is different in terms of both the phase-matching and the divergence. In typical experiments on high harmonic generation, the geometry of the experimental setup suppresses the so-called 'long' trajectories and favours the short ones. To account for this experimental aspect and eliminate from the theoretical spectrum the experimentally unobserved interference effects between the short and long trajectories contributions, which could, in principle, wash out the interference effects between the contributions from the various channels, the absorbing radius, i.e. the radius at which the CAP starts to be different from zero, has been set to approximately coincide with the classical quiver amplitude of the highest return kinetic energy electrons $r_{HHG} = \frac{E_{max}}{\omega^2}$. At this kinetic energy of return the two sets of trajectories merge into one; shorter trajectories which contribute to lower emission photon energies are not absorbed while the longer trajectories, which also contribute to lower high harmonic energies, are absorbed by the CAP. Therefore, the CAP acts as a filter which smoothly removes the long trajectories contribution from the time-dependent calculated dipole $D(t)$, suppressing the signal after the most energetic $\approx U_p$ electron trajectory. The CAP used in this calculation has a strength $\eta = 0.0005$. The calculations have been performed using a parabolic-linear B-spline knot sequence with a radial box radius

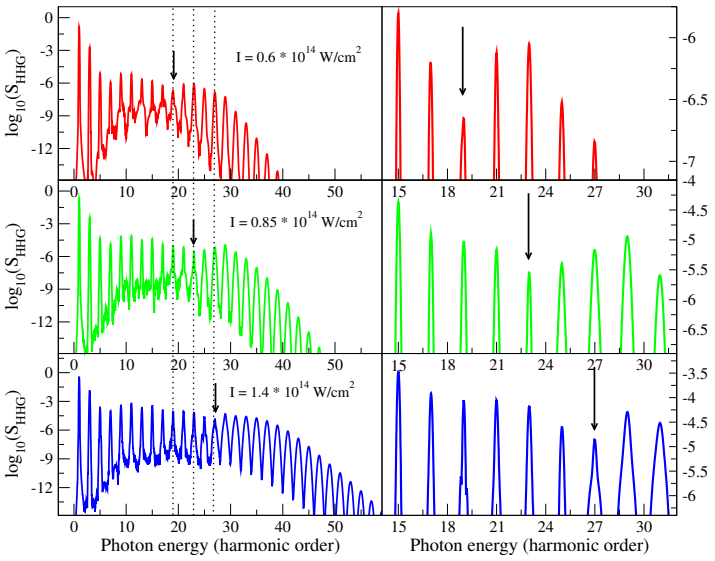


Fig. 1 ADC(1) high harmonic generation emission spectrum of the CO_2 molecule interacting with an IR field. The time duration 70 fs and the central wavelength is 800 nm. The laser field is linearly polarised along the molecular axis. Top panel – the peak intensity of the IR laser pulse used is $0.6 \times 10^{14}\,\mathrm{W/cm^2}$; central panel – the peak intensity of the IR laser pulse used is $0.85 \times 10^{14}\,\mathrm{W/cm^2}$; bottom panel – the peak intensity of the IR laser pulse used is $1.4 \times 10^{14}\,\mathrm{W/cm^2}$.

$R_{max} = 120$ a.u. and 180 radial grid points. The knot spacing in the linear region allows us to accurately describe photo-electron states within the range of kinetic energies of interest in the HHG process.

The cutoff is determined by the maximum recollision energy E_{kin} and by the ionization potential I_p as $\Omega_{\text{cutoff}} = 3.17U_p + 1.32I_p$. This means that, as the ionization energy of the HOMO-2 channel in CO_2 is 4.3 eV higher than that of the HOMO channel, the corresponding harmonic cutoff is shifted by nearly 6 eV.

In the following calculation we have used the first-order method of the ADC-hierarchy, namely ADC(1)[43,94]. The HHG spectrum, which is calculated via the expectation value of the electric dipole moment $z(t)$[95], reads

$$S_{hhg}(\omega) = \frac{1}{20}\frac{1}{3\pi c^3}\left|\int_{-\infty}^{\infty}[\frac{d^2}{dt^2}\langle z\rangle(t)]e^{-i\omega t}\,dt\right|^2 \qquad (37)$$

The ADC(1) high harmonic spectrum of the CO_2 molecule has been calculated for three different laser peak-intensities, namely $I_1 = 0.6\times10^{14}\,\text{W/cm}^2, I_2 = 0.85\times10^{14}\,\text{W/cm}^2, I_3 = 1.4\times10^{14}\,\text{W/cm}^2$. The laser pulses used in the calculation have a carrier frequency of $\omega = 0.057$ a.u. (800 nm) and a full width at half maximum (FWHM) pulse duration of $\tau = 2900$ a.u. (70 fs). The time-step and the maximum Krylov space dimension K used in the calculation are equal to 0.2 a.u. (1/500 of the IR period) and $K = 40$ respectively, at which value the convergence of our final results has been obtained.

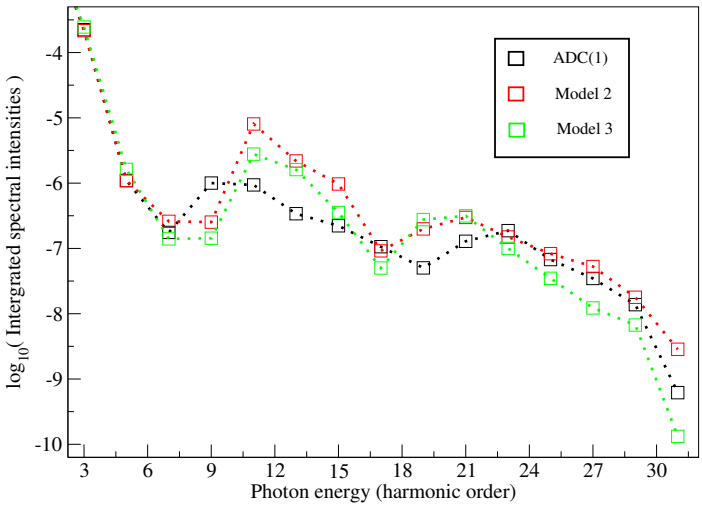


Fig. 2 Black squares – high harmonic generation emission spectrum of the CO_2 molecule interacting with an IR field, calculated using the full ADC(1) model with both correlation-driven and dipole interchannel couplings included; red squares – high harmonic generation emission spectrum of the CO_2 molecule interacting with an IR field, calculated using *model-2*: ADC(1) without correlation-driven interchannel couplings; green squares – high harmonic generation emission spectrum of the CO_2 molecule interacting with an IR field, calculated using *model-3* (independent-electron approximation): ADC(1) without correlation-driven and dipole interchannel couplings. The peak intensity of the IR laser pulse used is $0.6\times10^{14}\,\text{W/cm}^2$, the time duration 70 fs and the central wavelength 800 nm.

The calculated ADC(1) HHG spectra are shown in Fig. 1. As can be seen, the *ab-initio* calculations performed here present a clear minimum in the high harmonic spectrum of CO_2, which shifts to higher orders with increasing intensity, from H_{19} at $I_1 = 0.6\times10^{14}\,\text{W/cm}^2$ to H_{27} at $I_3 = 1.4\times10^{14}\,\text{W/cm}^2$. Varying the intensity of the fundamental field allows one to vary the relative phase of the high-harmonic emission channels, thereby controlling the photon energy at which the destructive interference occurs. Therefore, the main features of the CO_2 molecule HHG spectra, i.e. the position of the dynamical minimum and its field intensity dependence, are found to be reproduced by the B-spline ADC(1) calculations in very good agreement with the various experiments which have been performed during the past few years[21,29–31,49]. Indeed, experiment[21] confirms that the harmonic minimum shifts approximately linearly with intensity.

In Table 2 the calculated positions of the dynamical minimum in the CO_2 HHG spectrum for the three different peak intensities of the IR laser field and for the three different levels of theoretical approximation are summarized and compared with the experimental values measured in[25]. Moreover, as can be seen from Table 2, the correlation-driven interchannel couplings (Eq. (2)) play an important role in determining the structure of the spectra and the position of the minimum in general depends on their inclusion in the simulation. Our results show that the dipole interchannel couplings do not change the position of the minima, within the range of ionizing field parameters used in this work. Although, within the range of field intensities used here, this observable is not affected by the couplings of Eq. (1), the electron rearrangement within the ion caused by laser-driven dipole couplings between the different ionic states i and j, still modifies the ultrafast multi-channel dynamics leading to a change of the harmonic intensities in the total HHG spectrum (see Fig. 2) as well as to a change of the channel-resolved harmonics intensities and phases (see Section 4).

Table 2 Comparison between the experimental[25] and the calculated positions of the dynamical minimum in the CO_2 HHG spectrum for different peak intensities of the IR laser field and for different levels of theoretical approximation

IR peak-intesity	ADC(1)	*Model-2*	*Model-3*	Exp[25]
$0.6\times10^{14}\,\text{W/cm}^2$	19	17	17	19
$0.85\times10^{14}\,\text{W/cm}^2$	23	21	21	23
$1.4\times10^{14}\,\text{W/cm}^2$	27	25	25	27

In Fig. 2, the integrated high harmonic spectra of CO_2, calculated with respectively ADC(1), *model-2* and *model-3*, are shown for the case of the $I_1 = 0.6\times10^{14}\,\text{W/cm}^2$ peak intensity IR laser field. As can be observed, the ADC(1) calculated minimum is shifted to a higher harmonic order, 19, with respect to the minimum calculated with the other two models, which appears at harmonic order 17. Moreover, the ADC(1) plateau harmonics show a smaller intensity with respect to both the *model-2* and *model-3* ones (up to the harmonic order 21). Close to the cutoff region (harmonic orders 23, 25 and 27) the inclusion of the dipole couplings between the ionic channels increases the harmonic intensities with respect to the result obtained with *model-3*, whereas the addition of the correlation-driven interchannel couplings does not

lead to significant modifications to the *model-2* harmonic intensities.

4 Channel-resolved HHG intensities and relative phases: effects of correlation-driven and dipole interchannel couplings

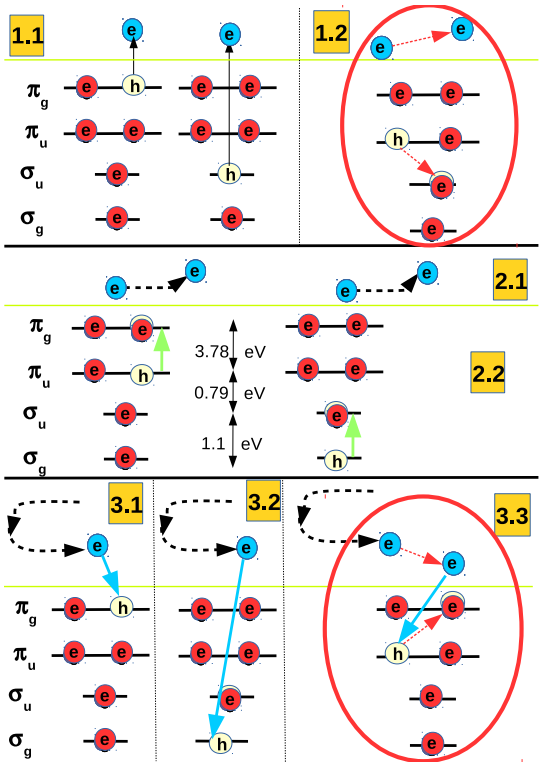


Fig. 3 Schematic illustration of the HHG process in CO_2 within the ADC(1) description (spin states are excluded). (1.1) The electron is tunnel-ionized mainly from the π_g and σ_u orbitals by the strong-field driving pulse. Correlation assisted tunneling (1.2), where the exchange of energy between the tunnel ionised electron and the parent ion happens just after tunnel ionisation, is also possible. As illustrated in the figure, in this case the π_u channel interacts with the σ_u one and the ionised electron is accelerated. In the second step, the electron is driven back to the ion by the oscillating electric field (2.1) and laser induced dipole transitions between the π_g, σ_u and the π_u, σ_g orbitals respectively, can also populate the originally unpopulated $1^2\Pi_u$ and $1^2\Sigma_g^+$ excited ionic states (2.2) (Eq. (1)). In the third step, the electron recombines with the ion in two different ways: the electron recombines with either the very same holes generated in step 1 (3.1) or with the holes generated in step 2.2 (3.2), with no further multi-channel interaction; alternatively, before recombining, the electron exchanges energy with the ion by promoting ionic transitions between occupied and empty molecular orbitals (3.3). Processes 1.2 and 3.3 are mediated by correlation-driven interchannel couplings (Eq. (2)). All the 4 molecular orbitals π_g, π_u, σ_u and σ_g contribute to the Coulomb interaction and interact with each other in step 3.3. As an example, the case where the π_u channel interacts with the π_g one is illustrated in this figure.

A schematic of the HHG process for CO_2 within the ADC(1) description is shown in Fig. 3. Steps 1.1, 2.1 and 3.1 are the same as in the well-known three-step model[26,50,96]. In step (1.1), either the π_g or the σ_u electrons are predominantly tunnel ionized by the IR strong-field pulse and in step (2.1), the liberated electron moves in the continuum driven by the strong-field pulse. In the third step the electron recombines with the parent ion and HHG radiation is emitted. During this last step the returning electron can either recombine with the original molecular orbital it had been previously tunnel ionised from (3.1), or alternatively can recombine with a different excited ionic state, $1^2\Pi_u$ or $1^2\Sigma_g^+$, where the hole is instead in either the π_u or σ_g molecular orbitals respectively (3.2, 3.3). In the case studied in this work where CO_2 molecules are aligned along the laser driving field polarization direction, the HOMO and HOMO-2 molecular orbitals are not directly accessed via tunnel ionization[25,97,98] and can only contribute indirectly to the HHG process. These two excited ionic states can be populated during the IR laser field subcycle via two different mechanisms, which interplay with each other. The first mechanism (2.2) consists of electron rearrangement within the parent ion caused by dipole-induced Rabi-like oscillations between ionic states i and j coupled by the laser electric field. In the case of CO_2 molecules aligned along the laser driving field polarization direction, this mechanism couples ionic states with opposite parity and same axial quantum number, i.e. π_g is coupled to π_u and σ_u is coupled to σ_g.

In the second mechanism (1.2, 3.3) the returning electron and the ion exchange energy via the electron-electron interaction (correlation-driven interchannel couplings) just before recombination or just after tunnel ionisation (correlation assisted tunneling), so that the electron can recombine with any of the ionic states participating in this interaction. Since the electron-electron Coulomb interaction mediating this exchange of energy can change the symmetry of both the ionic and returning electron states involved, all the 4 molecular orbitals (channels) included in this work (π_g, π_u, σ_u, σ_g) interact with each other in this step. The two-body character of the electron-electron interaction involved in steps 1.2 and 3.3 exists only in many-body, but not in single-electron, theories. Due to the fact that before recombination the ionic system can have a hole in any of the 4 energetically accessible molecular orbitals, correlation-driven interchannel couplings can either excite or de-excite the ionic system before recombination. When the returning electron is highly energetic ionic excitations are induced more efficiently. Correlation-driven ionic excitation mainly happens when the returning electron is close to the parent ion and can exchange energy with it. In the vicinity of the parent ion the returning electron wavepacket is modified by a short-range potential which is highly system- and state-dependent, which is reflected in the emitted harmonic spectrum. The above effects can only be captured by a full *ab initio* simulation which accurately represents two-electron couplings (see Eq. (2)) for all the ionic channels energetically accessible in the HHG process and for the returning electron wave-functions describing all the possible recombining kinetic energies.

The interchannel couplings of Eq. (2) change the phase of both the photoelectron and ionic wave-functions at the moments of tunneling ionisation and recombination, giving rise to a change of phase of the dipole transition matrix elements (Eq. (38)) and consequently of the channel-resolved harmonics. Moreover, also the amplitudes of both the returning electron wavepacket and ionic state populations is affected by Eq. (2), resulting again

in a change of amplitude of the corresponding dipole transition matrix elements (Eq. (38)). Both the phase and the amplitude of each channel contributions to the overall HHG spectrum are modified by Eq. (2). These changes, mapped onto the amplitude modulation in the total harmonic spectrum, encode how the correlation-driven interchannel couplings, as well as the interplay between them and the laser-driven dipole ones, modify the multi-channel sub-cycle electron dynamics induced by the strong IR ionising field, including the opening of new ionization-recombination channels.

In order to show this, we calculated, additionally to the total HHG spectra, the orbital-resolved contributions to the total HHG spectrum for each of the 3 different models. The orbital resolved spectra that are presented in the following are obtained by performing the multi-channel simulations, at the various levels of approximation described above, and calculating the contributions to the induced dipole coming from the excited configurations corresponding to each specific occupied orbital **i** respectively:

$$D_{\mathbf{i}}(t) = \langle \Psi_{\mathbf{i}a,0}(t) \mid \hat{D} \mid \Psi_{\mathbf{i}b,0}(t) \rangle , \tag{38}$$

where

$$\mid \Psi_{\mathbf{i}a,0}(t) \rangle = C_0(t) \mid \Psi_0 \rangle + \sum_a C_{\mathbf{i},a}(t) \mid \Phi_{\mathbf{i}}^a \rangle . \tag{39}$$

Therefore the single-orbital contributions obtained in *model-3* are of the pure single active electron flavour, while the contributions obtained within the ADC(1) model and within *model-2* take into account, at different levels of accuracy, the effect of the interchannel couplings of Eq. (2) and Eq. (1) on each single-orbital resolved spectrum.

In Fig. 4, the integrated orbital-resolved high harmonic generation spectral intensities of CO_2, calculated with respectively ADC(1), *model-2* and *model-3*, are shown for the case of the $I_1 = 0.6 \times 10^{14}\,\mathrm{W/cm^2}$ peak intensity IR laser field.

The relative phases between contributions to the total HHG spectrum from the different emission channels i and j can be extracted from the calculation in the following way:

$$\Phi_{\mathbf{i},\mathbf{j}} = \arccos\left(Re\left(\frac{\tilde{D}_{\mathbf{i}}(\omega)\tilde{D}_{\mathbf{j}}^{*}(\omega)}{\mid \tilde{D}_{\mathbf{i}}(\omega) \mid\mid \tilde{D}_{\mathbf{j}}(\omega) \mid} \right) \right) . \tag{40}$$

In Fig. 5, the cosine of the phase differences between the different channel contributions are shown for the cases of the ADC(1), *model-2* and *model-3* calculations respectively.

Let us first discuss the results in Fig. 4 and Fig. 5 obtained using the independent-electron model, i.e. *model-3*. Within *model-3*, both the influence of the laser field (dipole interchannel couplings) and the effect of the interaction with the ionised electron (correlation-driven interchannel couplings) on the bound electrons in the CO_2 parent ion are neglected. Since, in contrast to *model-2*, laser-induced transitions in the molecular ion are not considered here and therefore the high-harmonic signal is a coherent sum of the signals generated by ionising from and recombining to the same molecular orbital. The HOMO channel (black curve) dominates the emission for lower harmonics up to harmonic number 15; the HOMO-2 channel (green curve) has a comparable contribution (the difference of the contributions is less

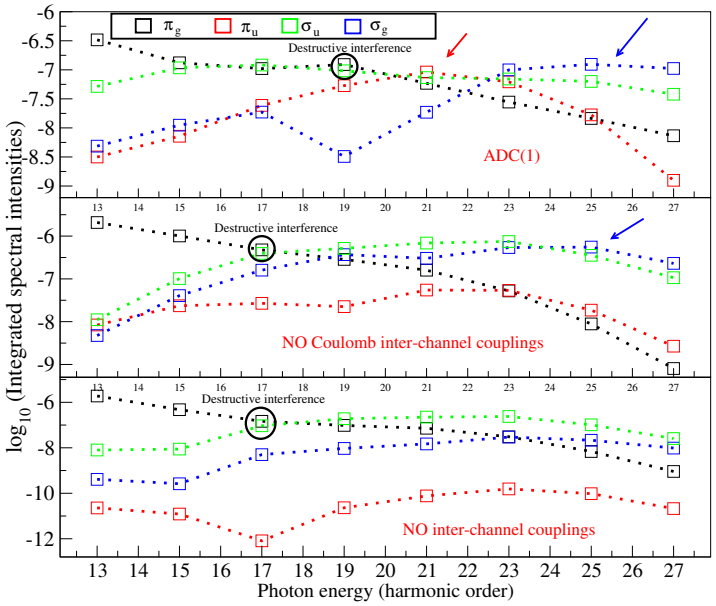


Fig. 4 Orbital resolved ADC(1) high harmonic generation emission integrated spectral intensities of the CO_2 molecule interacting with an IR field. Top panel – full ADC(1) model; central panel – *model-2*: ADC(1) without correlation-driven interchannel couplings; bottom panel – *model-3* (independent-electron approximation): ADC(1) without correlation-driven and dipole interchannel couplings. Black curve – intensity of the contribution to the HHG spectrum from the HOMO orbital, π_g; red curve – intensity of the contribution to the HHG spectrum from the HOMO-1 orbital, π_u; green curve – intensity of the contribution to the HHG spectrum from the HOMO-2 orbital, σ_u; blue curve – intensity of the contribution to the HHG spectrum from the HOMO-3 orbital, σ_g. The peak intensity of the IR laser pulse used is $0.6 \times 10^{14}\,\mathrm{W/cm^2}$, the time duration 70 fs and the central wavelength 800 nm.

than an order of magnitude) starting from the harmonic number 17 up to 21, taking over the HOMO contribution at the harmonic number 19.

The cutoff in the harmonic spectrum is determined by the maximum energy of the recombining electron, which is fixed by the electric field amplitude and the laser frequency, plus the ionization potential I_p of the state into which it recombines; thus, contribution from the deepest orbital with the highest I_p naturally becomes relevant beyond the cutoffs of the harmonics associated with the lower I_p channels. In the case of *model-3*, the HOMO-3 channel gives negligible contribution with respect to the HOMO-2 channel, i.e. its contribution is always more than an order of magnitude less, up to the harmonic cutoff (harmonic order 27) where the two contributions have the same order of magnitude. Moreover, the HOMO-1 channel (red curve) shows even more negligible contribution throughout the spectrum, its intensity being more than three orders of magnitude less than the one of the most contributing channel at each harmonic order. This could be expected because of the following: ionization from the HOMO orbital along or perpendicular to the molecular axis will be suppressed[36,37], owing to the destructive interference of currents from the orbital 'lobes' with opposite signs. This effect weakens the contribution of the HOMO orbital, which otherwise would be completely dominant due to the much lower ionization po-

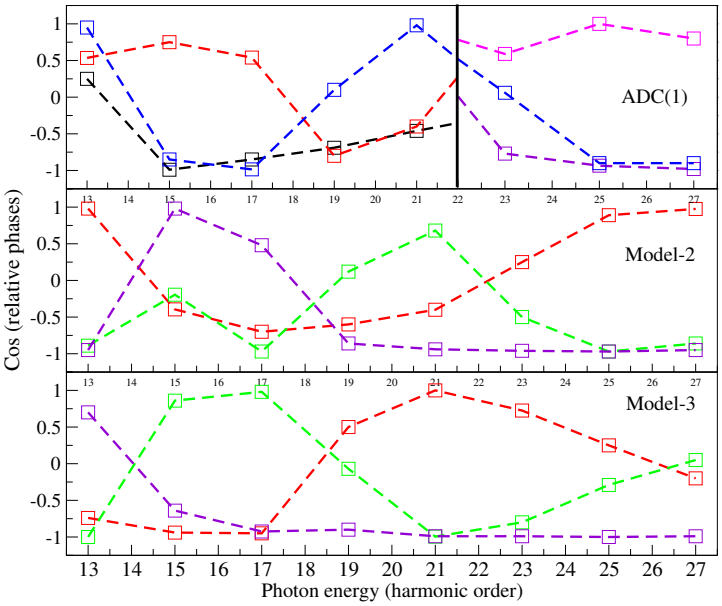


Fig. 5 Cosine of the relative phases between the contributions to the HHG emission from the channels of CO_2. Top panel – full ADC(1) model; central panel – *model-2*: ADC(1) without correlation-driven interchannel couplings; bottom panel – *model-3* (independent-electron approximation): ADC(1) without correlation-driven and dipole interchannel couplings. Black curve – $\cos\left(\Phi_{\pi_g,\pi_u}\right)$ (HOMO and HOMO-1 orbitals); red curve – $\cos\left(\Phi_{\pi_g,\sigma_u}\right)$ (HOMO and HOMO-2 orbitals); green curve –$\cos\left(\Phi_{\pi_g,\sigma_g}\right)$ (HOMO and HOMO-3 orbitals); blue curve – $\cos\left(\Phi_{\pi_u,\sigma_u}\right)$ (HOMO-1 and HOMO-2 orbitals); magenta curve – $\cos\left(\Phi_{\pi_u,\sigma_g}\right)$ (HOMO-1 and HOMO-3 orbitals); violet curve – $\cos\left(\Phi_{\sigma_u,\sigma_g}\right)$ (HOMO-2 and HOMO-3 orbitals). In the top panel, the two regions corresponding to harmonic orders smaller than 23 are separated by a vertical black line. In each region we plot the relative phases between the channels which give the predominant contribution to the spectrum, namely $\cos\left(\Phi_{\pi_g,\pi_u}\right)$, $\cos\left(\Phi_{\pi_g,\sigma_u}\right)$ and $\cos\left(\Phi_{\pi_u,\sigma_u}\right)$ for harmonic orders smaller than 23 and $\cos\left(\Phi_{\pi_u,\sigma_u}\right)$, $\cos\left(\Phi_{\pi_u,\sigma_g}\right)$ and $\cos\left(\Phi_{\sigma_u,\sigma_g}\right)$ for harmonic order 23, 25 and 27. The peak intensity of the IR laser pulse used is $0.6\times10^{14}\,\mathrm{W/cm^2}$, the time duration 70 fs and the central wavelength 800 nm.

tential. For channel A (HOMO-1), the molecular orbital favours ionization perpendicular to the molecular axis, while for channel B (HOMO-2) it favours ionization parallel to the molecular axis. At the independent-electron level of approximation the angular variation of ionization rates and recombination dipoles are such that high-harmonic emission for molecules aligned along the laser driving field polarization direction is dominated by the channels corresponding to HOMO and HOMO-2 (as opposed to the perpendicular alignment case where it would be dominated by the HOMO and HOMO-1 channels) [25,97,98]. Therefore, within the single active electron approximation, it is a good approximation to consider only the two channels given by HOMO and HOMO-2 when studying high harmonic emission spectra of CO_2 molecules aligned along the driving laser field polarization direction.

The total spectrum (Fig. 2) records the relative phase between the channels by mapping it into the amplitude modulations. As can be seen in Fig. 5, within *model-3* the minimum at harmonic order 17 in the total spectrum corresponds to the destructive interference between the HOMO and HOMO-2 channels. At the same harmonic order, the contribution from HOMO-3 interferes constructively and destructively with the one from HOMO and HOMO-2 respectively, but this interference does not affect the amplitude modulation of the total HHG spectrum as the intensity of the HOMO-3 channel is more than an order of magnitude less than both the HOMO and HOMO-2 intensities.

Within the *model-2* orbital resolved spectrum, the influence of the laser field on the bound electrons in the CO_2 ion (dipole interchannel couplings) is included in the calculations, while the effect of the interaction between the ionised electron and the parent ion (correlation-driven interchannel couplings), on the latter, is still neglected. While the HOMO channel (black curve) still dominates the emission for lower harmonics up to harmonic order 15, differently from *model-3* here both the HOMO-2 (green curve) and the HOMO-3 (blue curve) channels give a comparable contribution to the HOMO channel for the harmonic orders 17 and 19 and they are both larger than the HOMO contribution for the higher harmonics starting from order 21. The spectral intensities from the HOMO-2 and HOMO-3 channels have the same order of magnitude starting from the harmonic order 17 up to the overall harmonic cutoff, where HOMO-3 becomes the channel contributing most (at harmonic orders 25 and 27). Therefore, the dipole interchannel coupling between the HOMO-2 and HOMO-3 channels driven by the IR electric field increases the contribution of the lowest I_p HOMO-3 channel.

Mechanism 2.2 (see Fig. 3) is responsible for the increase of the amplitude of the HOMO-3 channel. Due to the dipole couplings between the π_g and π_u as well as between the σ_u and σ_g channels, the intense IR electric field causes, during the time between ionisation and recombination, transitions within the parent ion between the tunnel ionised orbitals (π_g, σ_u) and the ones undepleted in *model-3* (π_u, σ_g) respectively. These transitions increase the population of the first $1^2\Pi_u$ and third $1^2\Sigma_g^+$ ionic excited states at the time of recombination, allowing the returning electron to recombine with an ionic state where the hole is now in either the π_u or σ_g molecular orbitals and therefore leading to an enhancement of the harmonics amplitude for these channels throughout the spectrum. Although the intensity of the HOMO-1 channel (red curve) is also considerably increased by this mechanism, even within the *model-2* framework its contribution is, at the laser intensity considered, negligible with respect to the most contributing channels throughout the spectrum.

As can be seen in Fig. 5, the minimum at harmonic order 17 in the total HHG spectrum (Fig. 2) mainly corresponds to the destructive interference between the HOMO and the HOMO-2 channels; at harmonic order 17 the values of the two spectral intensities are very close to each other (Fig. 4) and $\cos\left(\Phi_{\pi_g,\sigma_u}\right)$ is negative and equal to -0.7 (Fig. 5). However, although the value of the spectral intensity for the HOMO-3 channel is smaller than that of the HOMO and HOMO-2 channels, the HOMO-3 channel influences the harmonic emission and contribution to the minimum shape also comes from its destructive and constructive interferences with the HOMO and HOMO-2 channels respectively (Fig. 5).

As in the case of the *model-2* and *model-3* calculations, in the ADC(1) orbital resolved spectrum the HOMO channel (black curve) also dominates the emission for low order harmonics up

to harmonic number 13; the emission intensity from the HOMO-2 channel (green curve) gives a comparable contribution for the harmonic numbers 15, 17 and 19 and it takes over the HOMO intensity for the higher order harmonics. In contrast to the independent-electron (*model-3*) and the *model-2* results, within the ADC(1) framework, the harmonic emission from the HOMO-1 channel (red curve) shows non-negligible contribution for harmonic orders 19, 21 and 23, reaching its maximum specifically at harmonic number 21 where it becomes the major contributing channel. The contribution of the HOMO-3 channel (blue curve) here is totally irrelevant up to harmonic order 23, from which point HOMO-3 becomes the major contributing channel up to the harmonic cutoff. Below the position of the minimum and close to the harmonic cutoff, the amplitude of the total HHG spectrum is predominantly the result of the contributions from two channels; specifically the HOMO and HOMO-2 channels at harmonic orders 15 and 17 and the HOMO-2 and HOMO-3 ones at harmonic orders 25 and 27. Conversely, for harmonic orders 19, 21 and 23, the spectral intensities from three channels have the same order of magnitude and therefore give comparable contribution to the total HHG spectrum. The overall harmonic amplitudes at orders 19 and 21 are the result of the interference between the HOMO, HOMO-1 and HOMO-2 channels. At harmonic order 23, HOMO-1, HOMO-2 and HOMO-3 are the main contributing channels instead. Therefore, in the top panel of Fig. 5, for harmonic orders smaller than 23 the three curves corresponding to $\cos\left(\Phi_{\pi_g,\pi_u}\right)$, $\cos\left(\Phi_{\pi_g,\sigma_u}\right)$ and $\cos\left(\Phi_{\pi_u,\sigma_u}\right)$ respectively are plotted, while for harmonic order 23, 25 and 27 we plot the curves corresponding to $\cos\left(\Phi_{\pi_u,\sigma_u}\right)$, $\cos\left(\Phi_{\pi_u,\sigma_g}\right)$ and $\cos\left(\Phi_{\sigma_u,\sigma_g}\right)$. In Fig. 5, the two regions are separated by a vertical black line.

As can be seen in Fig. 5, also in the ADC(1) calculation the minimum at harmonic order 19 in the total spectrum (Fig. 2) mainly corresponds to the destructive interference between the HOMO and the HOMO-2 channels; at harmonic order 19 the values of the two spectral intensities are very close to each other (Fig. 4) and $\cos\left(\Phi_{\pi_g,\sigma_u}\right)$ is negative and equal to -0.8 (Fig. 5). However, differently from the *model-2* and *model-3* results, in this case the HOMO-1 channel significantly contributes to the harmonic emission process and consequently the minimum shape is also determined by the destructive and constructive interferences between the HOMO-1 channel and the HOMO and HOMO-2 channel contributions respectively (Fig. 5).

These results show that interchannel couplings can play an important role in understanding the relevance of multi-orbital effects during high-harmonic generation (HHG), increasing the contribution of ionization channels that would otherwise be negligible in an independent-electron model and also significantly changing the phase differences between the channel resolved harmonics as well as their resulting interference. In general, the population of an ionic channel at the end of the ionising pulse does not map directly to its relevance in the HHG mechanism. Therefore, the argument of low ionization probability by the end of the pulse is not sufficient to justify ignoring multi-channel contributions, such as the ones from the $HOMO-1$ and $HOMO-3$ orbitals in CO_2 in the aligned linearly polarised case (whose contributions had been neglected in previous works[21,25,29,30,49,61,62]). While, after the end of the pulse, their populations are relatively small, these channels play, indirectly through the interplay between dipole and correlation driven interchannel couplings, an important role in the sub-cycle many-electron dynamics quantitatively contributing to the resulting total HHG spectrum. As a result of this, within the range of field parameters used in this work we have found that the calculated shape and position of the dynamical minimum in the HHG spectrum of CO_2 changes depending on whether or not correlation-driven interchannel couplings are taken into account (see Fig. 2 and Table 2) and that neglecting them can also lead to large modifications of up to one order of magnitude in the HHG yield, especially in the plateau region (see Fig. 2).

5 Conclusions

In this work we have described the molecular HHG process using the *ab initio* TD B-spline ADC(1) many-body approach and studied the impact of the full inclusion of the correlation-driven interchannel couplings on the HHG spectrum of the CO_2 molecule. Our results show that electron correlation modifies the multi-channel sub-cycle electron dynamics induced in the parent ion by the strong IR ionizing field, interplaying with the laser-driven ionic dipole interchannel couplings and effectively opening new ionization-recombination channels. This interplay shapes the total molecular HHG spectrum. The argument of low ionization probability by the end of the pulse is thus not sufficient to justify ignoring multi-channel contributions, such as the ones from the $1^2\Pi_u$ and $1^2\Sigma_g^+$ excited ionic states in CO_2 in the aligned linearly polarised case. Indeed, the contribution of these channels to the HHG emission during the interaction between the molecule and the strong IR laser field pulse is not small and has to be taken into account in order to correctly predict the position of the dynamical HHG minimum. Therefore, we conclude that inclusion of such commonly neglected many-electron effects into the theoretical interpretation of molecular HHG spectra is essential in order to correctly extract attosecond electron dynamics in the ion (e.g. hole migration[99]) by any HHG-based spectroscopic scheme[15,19,20,25,63,100,101]. By showing how new electron-electron correlation assisted channels modify the molecular high harmonic response, this work provides new important insight into the electron dynamics underlying strong-field ionization of molecules and how these dynamics manifest in highly nonlinear response. We expect that these findings will have a major impact on the design and interpretation of future molecular HHG-based attosecond experiments.

This work was funded by EPSRC/DSTL MURI grant EP/N018680/1.

Conflict of interest

There are no conflicts to declare

References

1 M. Hentschel , R. Kienberger, Ch. Spielmann, G. A. Reider, N. Milosevic, T. Brabec, P Corkum, U. Heinzmann, M. Drescher and F. Krausz, Nature, 2001, **414**, 509.

2 F. Krausz and M. Ivanov, Rev. Mod. Phys., 2009, **81**, 163.

3 L. Cederbaum and J. Zobeley, Chem. Phys. Lett., 1999, **307**, 205.

4 J. Mauritsson, P. Johnsson, E. Mansten, M. Swoboda, T. Ruchon, A. L'Huillier, and K. J. Schafer, Phys. Rev. Lett., 2008, **100**, 073003.

5 P. Eckle, A. N. Pfeiffer, C. Cirelli, A. Staudte, R. Dörner, H. G. Muller, M. Büttiker, and U. Keller, Science, 2008, **322**, 1525.

6 C. Ott, A. Kaldun, P. Raith, K. Meyer, M. Laux, J. Evers, C. H. Keitel, C. H. Greene, and T. Pfeifer, Science, 2013, **340**, 716.

7 M. Schultze, K. Ramasesha, C. Pemmaraju, S. Sato, D. Whitmore, A. Gandman, J. S. Prell, L. J. Borja, D. Prendergast, K. Yabana, D. M. Neumark, and S. R. Leone, Science, 2014, **346**, 1348.

8 M. C. H. Wong, A.-T. Le, A. F. Alharbi, A. E. Boguslavskiy, R. R. Lucchese, J.-P. Brichta, C. D. Lin, and V. R. Bhardwaj, Phys. Rev. Lett., 2013, **110**, 033006.

9 I. Petersen, J. Henkel, and M. Lein, Phys. Rev. Lett., 2015, **114**, 103004.

10 M. Drescher, M. Hentschel, R. Kienberger, M. Uiberacker, V. Yakovlev, A. Scrinzi, Th. Westerwalbesloh, U. Kleineberg, U. Heinzmann and F. Krausz, Nature, 2002, **419**, 803.

11 K. Schnorr, A. Senftleben, M. Kurka, A. Rudenko, L. Foucar, G. Schmid, A. Broska, T. Pfeifer, K. Meyer, D. Anielski, R. Boll, D. Rolles, M. Kübel, M. F. Kling, Y. H. Jiang, S. Mondal, T. Tachibana, K. Ueda, T. Marchenko, M. Simon, G. Brenner, R. Treusch, S. Scheit, V. Averbukh, J. Ullrich, C. D. Schröter and R. Moshammer, Phys. Rev. Lett., 2013, **111**, 093402.

12 E. Goulielmakis, Z. Loh, A. Wirth, R. Santra, N. Rohringer, V. S. Yakovlev, S. Zherebtsov, T. Pfeifer, A. M. Azzeer, M. F. Kling, S. R. Leone and F. Krausz, Nature, 2010, **466**, 739.

13 A. Wirth, M. T. Hassan, I. Grguras, J. Gagnon, A. Moulet, T. T. Luu, S. Pabst, R. Santra, Z. A. Alahmed, A. M. Azzeer, V. S. Yakovlev, V. Pervak, F. Krausz, and E. Goulielmakis, Science, 2011, **334**, 195.

14 C. Ott, A. Kaldun, L. Argenti, P. Raith, K. Meyer, M. Laux, Y. Zhang, A. Blattermann, S. Hagstotz, T. Ding, R. Heck, J. Madronero, F. Martin, and T. Pfeifer, Nature, 2014, **516**, 374.

15 J. Leeuwenburgh, B. Cooper, V. Averbukh, J. P. Marangos, and M. Ivanov, Phys. Rev. Lett., 2013, **111**, 123002.

16 G. Doumy, J. Wheeler, C. Roedig, R. Chirla, P. Agostini and L. F. DiMauro, Phys. Rev. Lett., 2009, **102**, 093002.

17 N. Dudovich, O. Smirnova, J. Levesque, Y. Mairesse, M. Yu. Ivanov, D. M. Villeneuve and P. B. Corkum, Nature Phys., 2006, **2**, 781.

18 E. A. Gibson, A. Paul, N. Wagner, R. Tobey, S. Backus, I. P. Christov, M. M. Murnane and H. C. Kapteyn, Phys. Rev. Lett., 2004, **92**, 033001.

19 J. Itatani, J. Levesque, D. Zeidler, H. Niikura, H. Pepin, J. Kieffer, P. Corkum, and D. Villeneuve, Nature (London), 2004, **432**, 867.

20 C. Vozzi, M. Negro, F. Calegari, G. Sansone, M. Nisoli, S. De Silvestri and S. Stagira, Nature Physics, 2011, **7**, 822-826.

21 T. Kanai, S. Minemoto, and H. Sakai, Nature (London), 2005, **435**, 470.

22 S. Baker, J. S. Robinson, C. A. Haworth, H. Teng, R. A. Smith, C. C. Chirila, M. Lein, J. W. G. Tisch and J. P. Marangos, Science, 2006, **312**, 424.

23 J. P. Marangos, S. Baker, N. Kajumba, J. S. Robinson, J. W. G. Tisch and R. Torres, Phys. Chem. Chem. Phys., 2008, **10**, 35-48.

24 C. Vozzi, R. Torres, M. Negro, L. Brugnera, T. Siegel, C. Altucci, R. Velotta, F. Frassetto, L. Poletto, P. Villoresi, S. De Silvestri, S. Stagira and J. P. Marangos, Appl. Phys. Lett., 2010, **97**, 241103.

25 O. Smirnova, Y. Mairesse, S. Patchkovskii, N. Dudovich, D. Villeneuve, P. Corkum, and M. Y. Ivanov, Nature (London), 2009, **460**, 972.

26 P. B. Corkum, Phys. Rev. Lett., 1993, **71**, 1994.

27 Y. Mairesse, J. Higuet, N. Dudovich, D. Shafir, B. Fabre, E. Mével, E. Constant, S. Patchkovskii, Z. Walters, M. Yu. Ivanov and O. Smirnova, Phys. Rev. Lett., 2010, **104**, 213601.

28 T. Morishita, A.-T. Le, Z. Chen, and C. D. Lin, Phys. Rev. Lett., 2008, **100**, 013903.

29 C. Vozzi, F. Calegari, E. Benedetti, J.-P. Caumes, G. Sansone, S. Stagira, M. Nisoli, R. Torres, E. Heesel, N. Kajumba, J. P. Marangos, C. Altucci and R. Velotta, Phys. Rev. Lett., 2005, **95**, 153902.

30 W. Boutu, S. Haessler, H. Merdji, P. Breger, G. Waters, M. Stankiewicz, L. J. Frasinski, R. Taieb, J. Caillat, A. Maquet, P. Monchicourt, B. Carre and P. Salieres, Nature Phys., 2008, **4**, 545-549.

31 X. Zhou, R. Lock, W. Li, N. Wagner, M. M. Murnane, and H. C. Kapteyn, Phys. Rev. Lett., 2008, **100**, 073902.

32 A. T. Le, T. Morishita and C. D. Lin, Phys. Rev. A, 2008, **78**, 023814.

33 V. H. Le, A. T. Le, R. H. Xie and C. D. Lin, Phys. Rev. A, 2007, **76**, 013414.

34 A. T. Le, X. M. Tong and C. D. Lin, Phys. Rev. A, 2006, **73**, 041402.

35 M. Lein, J. Phys. B, 2007, **40**, R135-R173.

36 X. M. Tong, Z. X. Zhao and C. D. Lin, Phys. Rev. Lett., 2002, **66**, 033402.

37 J. Muth-Bohm, A. Becker and F. H. M. Faisal, Phys. Rev. Lett., 2000, **85**, 2280-2283.

38 B. K. McFarland, J. P. Farrell, P. H. Bucksbaum, and M. Gühr, Science, 2008, **322**, 1232.

39 W. Li, X. Zhou, R. Lock, S.Patchkovskii, A. Stolow, H. C. Kapteyn and M. M. Murnane, Science, 2006, **322**, 1207-1211.

40 A.-T. Le, R. R. Lucchese, and C. D. Lin, J. Phys. B, 2009, **42**, 211001.

41 V. Averbukh, O.E. Alon and N. Moiseyev, Phys. Rev. A, 2001, **64**, 033411.

42 V. Averbukh, Phys. Rev. A, 2004, **69**, 043406.

43 M. Ruberti, V. Averbukh and P. Decleva, J. Chem. Phys., 2014, **141**, 164126.

44 A.-T. Le, R. R. Lucchese, S. Tonzani, T. Morishita, and C. D. Lin, Phys. Rev. A, 2009, **80**, 013401.

45 A. D. Shiner, B. E. Schmidt, C. Trallero-Herrero, P. B. Corkum,

J.-C. Kieffer, F. Legare and D. M. Villeneuve, J. Phys. B: At. Mol. Opt. Phys., 2012, **45**, 074010.
46 H. J. Wörner, H. Niikura, J. B. Bertrand, P. B. Corkum, and D. M. Villeneuve, Phys. Rev. Lett., 2009, **102**, 103901.
47 J. P. Farrell, L. S. Spector, B. K. McFarland, P. H. Bucksbaum, M. Guhr, M. B. Gaarde, and K. J. Schafer, Phys. Rev. A, 2011, **83**, 023420.
48 S. Minemoto, T. Umegaki, Y. Oguchi, T. Morishita, A.-T. Le, S. Watanabe and H. Sakai, Phys. Rev. A, 2008, **78**, 061402(R).
49 H. J. Wörner, J. B. Bertrand, P. Hockett, P. B. Corkum, and D. M. Villeneuve, Phys. Rev. Lett., 2010, **104**, 233904.
50 M. Lewenstein, Ph. Balcou, M. Yu. Ivanov, A. L'Huillier and P. B. Corkum, Phys. Rev. A, 1994, **49**, 2117.
51 J. Z. Kaminski and F. Ehlotzky, Phys. Rev. A, 1996, **54**, 3678.
52 O. Smirnova, A. S. Mouritzen, S. Patchkovskii, and M. Y. Ivanov, J. Phys. B, 2007, **40**, F197.
53 A. Abdurrouf and F. H. M. Faisal, Phys. Rev. A, 2009, **79**, 023405.
54 O. Smirnova, Spanner, M. Ivanov and M. Yu., Phys. Rev. A, 2008, **77**, 033407.
55 L. Torlina and O. Smirnova, Phys. Rev. A, 2012, **86**, 043408.
56 K. J. Schafer, B. Yang, L. F. Di Mauro, and K. C. Kulander, Phys. Rev. Lett., 1993, **70**, 1599.
57 K. C. Kulander, K. J. Schafer, and J. L. Krause, Int. J. Quantum Chem., 1991, **40**, 415.
58 J. Higuet, H. Ruf, N. Thiré, R. Cireasa, E. Constant, E. Cormier, D. Descamps, E. Mével, S. Petit, B. Pons, Y. Mairesse, and B. Fabre, Phys. Rev. A, 2011, **83**, 053401.
59 M. Awasthi, Y. V. Vanne, A. Saenz, A. Castro, and P. Decleva, Phys. Rev. A, 2008, **77**, 063403.
60 I. A. Ivanov and A. S. Kheifets, Phys. Rev. A, 2009, **79**, 053827.
61 P. Wei, P. Liu, J. Chen, Z. Zeng, X. Guo, X. Ge, R. Li and Z. Xu, Phys. Rev. A, 2009, **79**, 053814.
62 R. Torres, T. Siegel, L. Brugnera, I. Procino, J. G. Underwood, C. Altucci, R. Velotta, E. Springate, C. Froud, I. C. E. Turcu, S. Patchkovskii, M. Yu. Ivanov, O. Smirnova and J. P. Marangos, Phys. Rev. A, 2010, **81**, 051802.
63 B. D. Bruner, Z. Masin, M. Negro, F. Morales, D. Brambila, M. Devetta, D. Faccial, A. G. Harvey, M. Ivanov, Y. Mairesse, S. Patchkovskii, V. Serbinenko, H. Soifer, S. Stagira, C. Vozzi, N. Dudovich and O. Smirnova, Faraday Discuss., 2016, **194**, 369.
64 Walters, B. Zachary and O. Smirnova, Journal of Physics B: Atomic, Molecular and Optical Physics, 2010, **43**, 161002.
65 S. Pabst and R. Santra, Phys. Rev. Lett., 2013, **111**, 233005.
66 S. Pabst, L. Greenman, D. A. Mazziotti, and R. Santra, Phys. Rev. A, 2012, **85**, 023411.
67 A. E. Boguslavskiy, J. Mikosch, A. Gijsbertsen, M. Spanner, S. Patchkovskii, N. Gador, M. J. J. Vrakking and A. Stolow, Science, 2012, **335**, 1336.
68 J. Schirmer, Phys. Rev. A, 1982, **26**, 2395.
69 M. Ruberti, R. Yun, K. Gokhberg, S. Kopelke, L. S. Cederbaum, F. Tarantelli and V. Averbukh, J. Chem. Phys., 2013, **139**, 144107.
70 M. Ruberti, R. Yun, K. Gokhberg, S. Kopelke, L. S. Cederbaum, F. Tarantelli and V. Averbukh, J. Chem. Phys., 2014, **140**, 184107.
71 T. J. Park and J. C. Light, J. Chem. Phys., 1986, **85**, 5870.
72 A. F. Starace, in Handbuch der Physik, Vol. **31**, edited by W. Mehlhorn (Springer, Berlin, 1980), pp. 1-121.
73 J. Schirmer, Phys. Rev. A, 1991, **43**, 4647.
74 J. Schirmer and A. B. Trofimov, J. Chem. Phys., 2004, **120**, 11449.
75 E. Dalgaard, Int. J. Quantum Chem., 1979, **15**, 169.
76 A. Szabo and N. S. Ostlund, *Modern Quantum Chemistry: Introduction to Advanced Electronic Structure Theory*, Dover, New York, 1996.
77 F. Mertins, J. Schirmer and A. Tarantelli, Phys. Rev. A, 1996, **53**, 2153.
78 F. Mertins and J. Schirmer, Phys. Rev. A, 1996, **53**, 2140.
79 J. Schirmer and F. Mertins, J. Phys. B, 1996, **29**, 3559.
80 H. Bachau, E. Cormier, P. Decleva, J. E. Hansen and F. Martin, Rep. Prog. Phys., 2001, **64**, 1815.
81 U. V. Riss and H.-D. Meyer, J. Phys. B, 1993, **26**, 4503.
82 W. E. Arnoldi, Q. Appl. Math., 1951, **9**, 17.
83 R. A. Friesner, L. S. Tuckerman, B. C. Dornblaser, and T. V. Russo, J. Sci. Comput., 1989, **4**, 327.
84 H. Hennig, J. Breidbach, and L. S. Cederbaum J. Chem. Phys., 2005, **122**, 134104.
85 C. Leforestier, R. H. Bisseling, C. Cerjan *et al.*, J. Comput. Phys., 1991, **94**, 59.
86 G. Jolicard and E. Austin, J. Chem. Phys., 1991, **95**, 5056.
87 M. H. Beck, A. Jänckle, J. A. Worth, and H.-D. Meyer, Phys. Rep., 2001, **324**, 1.
88 B. N. Parlett, *The Symmetric Eigenvalue Problem* (Prentice-Hall, NJ, 1980).
89 M. Snir, S. Otto, S. Huss-Lederman, D. Walker, and J. Dongarra, *MPI: The Complete Reference* (The MIT Press Cambridge, Massachusetts, 1996).
90 B. Chapman, G. Jost and R. van der Pas, *Using OpenMP: Portable Shared Memory Parallel Programming* (The MIT Press Cambridge, Massachusetts, 2007).
91 J. V. Ortiz, Int. J. Quantum Chem., 2003, **95**, 593-599.
92 K. Kimura, S. Katsumata, Y. Achiba, T. Yamazaki, and S. Iwata, Handbook of HeI Photoelectron Spectra (Japan Scientific Societies Press, Tokyo, 1981).
93 MOLPRO, version 2012.1, a package of ab initio programs, H.-J. Werner, P. J. Knowles, G. Knizia, F. R. Manby, M. Schutz and others, see http://www.molpro.net.
94 E. R. Simpson, A. Sanchez-Gonzalez, D. R. Austin, Z. Diveki, S. E. E. Hutchinson, T. Siegel, M. Ruberti, V. Averbukh, L. Miseikis, C. S. Struber, L. Chipperfield and J. P. Marangos, New J. Phys., 2016, **18**, 083032.
95 A. Gordon and F. Kärtner, Opt. Express, 2005, **13**, 2941.
96 K. J. Schafer, B. Yang, L. F. DiMauro, and K. C. Kulander, Phys. Rev. Lett., 1993, **70**, 1599.
97 O. Smirnova, S. Patchkovskii, Y. Mairesse, N. Dudovich, D.

Villeneuve, P. Corkum and M. Y. Ivanov, Phys. Rev. Lett., 2009, **102**, 063601.

98 O. Smirnova, S. Patchkovskii, Y. Mairesse, N. Dudovich, and M. Y. Ivanov, Proc. Natl. Acad. Sci. U.S.A., 2009, **106**, 16556.

99 F. Calegari, D. Ayuso, A. Trabattoni, L. Belshaw, S. De Camillis, S. Anumula, F. Frassetto, L. Poletto, A. Palacios, P. Decleva, J. B. Greenwood, F. Martin, M. Nisoli, Science, 2014, **346**, 336-339.

100 P. M. Kraus, B. Mignolet, D. Baykusheva, A. Rupenyan, L. Horný, E. F. Penka, G. Grassi, O. I. Tolstikhin, J. Schneider, F. Jensen, L. B. Madsen, A. D. Bandrauk, F. Remacle, and H. J. Worner, Science, 2015, **350**, 790-795.

101 Y. Mairesse, A. de Bohan, L. J. Frasinski, H. Merdji, L. C. Dinu, P. Monchicourt, P. Breger, M. Kovacev, R. Tajeb, B. Carré, H. G. Muller, P. Agostini and P. Saliéres, Science, 2003, **302**, 1540.